AIMS Geosciences

AIMS Geosciences, 9(4): 652–671.
DOI: 10.3934/geosci.2023035
Received: 11 July 2023
Revised: 11 September 2023
Accepted: 25 October 2023
Published: 08 November 2023

http://www.aimspress.com/journal/geosciences

Research article

Measurement and characterization of infrasound waves from the March 25, 2023 thunderstorm at the near equatorial

Mario Batubara[1,*], Masa-yuki Yamamoto[2], Islam Hosni Hemdan Eldedsouki Hamama[3], Musthofa Lathif[1] and Ibnu Fathrio[4]

[1] Research Center for Space, National Research and Innovation Agency of Indonesia (BRIN), Indonesia
[2] Kochi University of Technology, Japan
[3] National Research Institute of Astronomy and Geophysics Department of Egyptian, Egypt
[4] Research Center for Climate and Atmosphere, BRIN, Indonesia

* **Correspondence:** Email: mari009@brin.go.id; Tel: 62213169059.

Abstract: Thunderstorm activity on March 25, 2023 provided a unique opportunity to study the mechanism of lightning events on changes in air pressure. In particular, this event made it possible to study changes in air pressure during thunderstorms using various instruments. This paper presented comprehensive results of infrasound, satellite data, weather radar and weather measurements at the ground during the storm. Observations of lightning events were confirmed using observational data from the International Space Station's Lightning Imaging Sensor (ISS LIS). This work estimated three spectral percentile values on infrasonic sensor data, time series interpolation of standard meteorology profiles, weather radar reflectivity and total radiant energy of lightning from ISS LIS observations during the day and night periods. As a result, during the investigation, it was seen that the recorded infrasound signal in the 0.6–0.8 Hertz (Hz) range was contaminated by background environmental noise, but in the 1–3 Hz band range it was consistent with the appearance of storms that produce high energy blows. Infrasound detection and electromagnetic lightning detection show good correlation up to a distance of 100 km from the infrasonic station. During a thunderstorm, the ISS LIS flight directly above the observation site detected more than 2,000 lightning events. In addition, the application of lightning detection from several independent instruments can provide a complete picture of the observed event.

Keywords: infrasound, thunderstorm, air pressure, lightning detection, electromagnetic discharge, meteorology

1. Introduction

Acoustic waves in the infrasound frequency range, i.e., sound waves that are inaudible below the lower limit of human hearing ability of 20 Hertz (Hz), are observed to propagate to a great distance from the point source. These waves have many sources, both natural and man-made, such as volcanic eruptions [1–5], earthquakes [6–10], tsunamis [11], thunder accompanied by lightning [12], waves related to mountains [13,14], bolides [15] and ocean waves [16], and can also be generated from artificial activities such as mining explosions [17], chemical explosions [18] and underground nuclear explosions [19]. Various institutions maintain detectors for monitoring purposes, such as thunderstorm studies [20], the International Monitoring System [21,22] or the Japan Infrasound Monitoring Network [23]. Many recent infrasound studies employ ground-based instruments used as geometric configurations.

Thunderstorms, in general, are often accompanied by lightning and its acoustic effects on the earth's atmosphere. Thunderstorms can be formed and developed in any geographic location but are most common in middle latitudes due to the process where two winds meet, forcing air upward and carrying moisture at a certain height to create a zone of low-pressure precipitation. The intensity of lightning depends on the intensity of the electric field in the cloud, which is closely related to the dynamic and microphysical processes in thunderstorms. Meanwhile, these dynamic and microphysical processes are directly related to the generation of storm clouds and precipitation particles, which ultimately determine the occurrence of heavy rain and severe weather [24–33]. The relationship between lightning and rainfall has long been recognized. Several techniques are used to determine the structure or mechanism of thunderstorms, including weather radar [34], weather station and photography. With the development of detection techniques, studies of this relationship have been carried out throughout the world. The ratio of average rainfall to the number of lightning flashes (i.e., rainfall field) was calculated in several regions [35]. Although this ratio varies around the world, it remains stable in local areas. Lightning and rainfall in winter storms in the eastern Mediterranean Sea were examined with Tropical Rainfall Measuring Mission (TRMM) observations [36]. A strong correlation between total flash rate and rainfall levels has been found. The TRMM Lightning Imaging Senor (LIS) collected lightning data from space from 1998–2015 onboard the TRMM satellite. In 2017 another LIS (built as a backup to the TRMM LIS) was launched into orbit and located on the International Space Station (ISS). More information about this ISS LIS is available in [37,38]. The comparison tropical maritime precipitation with and without lightning with ISS LIS observations was aimed to achieve an investigation of the interactions between precipitation, kinematics, and electrification during severe thunderstorm [28]. Observations using Doppler radar techniques provide a unique dataset for identifying and analyzing developing phenomena such as thunderstorms accompanied by high levels of rainfall or wind speeds. Obtained storm features can be utilized to highlight important characteristics such as severity, trajectory and structure evolution in a storm [39].

Based on satellite, radar and weather station observation, rainfall duration is usually defined as

rainfall events lasting for several hours in duration on a relatively small scale [40–42]. Automatic weather station data is used to verify surface variables (temperature, relative humidity, accumulated daily rain and average pressure on the surface) associated with the occurrence of thunderstorms. Radar technology is widely used to diagnose the components of the Mesoscale Convective System based on the reflectivity radar gradient [43]. Meanwhile, recent infrasonic observatory observations provide unique datasets that can provide good hurricane kinematics information.

The relationship of infrasound to thunderstorm events has been discussed in various theoretical and observational papers in the past. Observations related to lightning were first made in the 1960s [44,45]. They looked at the intensity of the audible spectrum, but then some work began to look at and investigate the acoustic domain in the infrasonic range where thunder accompanied by lightning can be heard at a distance of up to 30 km from the source location, and the induced acoustic pressure varies between 0.1 to 3 Pa at several kilometers. Furthermore, these pressure waves consist of a series of short pulses, approximately one to two seconds from measurements made with an air pressure sensor [46,47]. Adding a series of acoustic measurements of lightning, the physical mechanism of audible thunder is produced by acoustic radiation from a heated channel while acoustic in the low frequency range—infrasound, the mechanism of thunder, is caused by the conversion of the electrostatic field of thunder clouds into sound [48–50]. Along with thunderstorm events, lightning discharges are characterized by an electrostatic field that produces a reduction in atmospheric pressure within the charged cloud of approximately 0.05 to five Pa in the frequency range of 0.2–2 Hz.

A relatively large number of various types of observatories can be used to monitor thunderstorm events. This gives us the opportunity to combine results from multiple data sources. We analyzed data from satellite observations to confirm the occurrence of high-intensity thunderstorms in the region of our observation locations, as well as in situ measurements from basic meteo-measuring equipment, radio-based precipitation and infrasound wave detection at the ground. The background conditions of thunderstorms during the period of interest, as well as a description of the various observatories and data types used in this activity, are explained in section two. All observations used in this activity are systematically illustrated in section three. which is then continued in section four with a discussion of how observations relate to each other. Finally, we summarize the conclusions from the analysis of this activity in section five.

2. March 2023 thunderstorm background conditions

Infrasound generated from lightning during thunderstorms has been detected in the rainy month of March 2023 and the 25 of March thunderstorm (Figure 1), which passed just over the observation site. In Figure 1 (left), the activity of flashes has more than 2,000 activities detected in the image area and 258 flashes of activity detected in the area of interest (red rectangle). When a thunderstorm passes over the infrasound observation site, the ISS LIS simultaneously detects some lightning activity. These results can be seen in Figure 1 on the right where the number of flashes in the area of interest (red box) is 33, and the total number of flashes in the image is 117.

The location of the lightning strike was then estimated at a distance of around 200 kilometers during March 2023 based on the results of the ISS LIS monitoring (Figure 2, top panel). The longest period of reported lightning occurrences is 252 milliseconds, with the average value of the detected lightning pulse period being around 182.54 milliseconds (Figure 3). On March 25, 2023, a

thunderstorm event crossed the infrasound observation area, and the location of the lightning event was estimated 50 to 100 kilometers from the infrasound station (Figure 2, bottom panel). In addition to lightning observations observed by the ISS LIS, the duration of the electromagnetic discharge shock pulse ranged up to 1,200 ms in March 2023 (Figure 3, top panel). The duration of the observed shock pulses on March 25, 2023 was 522 ms for the highest period and 182.54 ms for the average period (Figure 3, bottom panel). In March 2023, the three highest lightning incidents were detected.

They were the highest lightning incidents detected in March 2023 and they occurred on the 13th, 17th, 20th, 22nd and 25th of March 2023, with incidents recorded at about 25, 65, 53, 37 and 33, respectively (Figures 2 and 3, top panel).

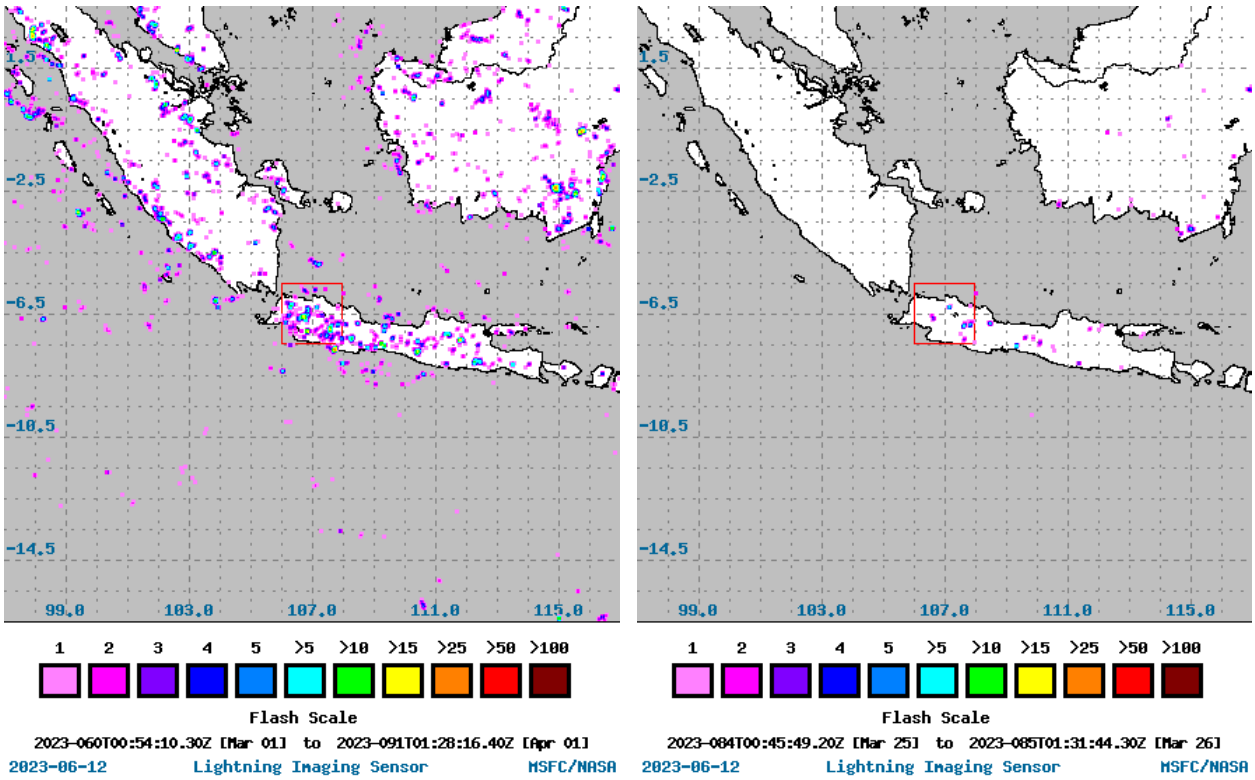

Figure 1. Lightning activity observed by ISS LIS. (Left) Lightning activity during rainy month of March 2023 (color describes lightning flash scale). Infrasound station located in the center of red rectangle. About 2,883 flashes occurred in the image where the number of flashes detected in the area of interest (red rectangle) is about 258. (Right) ISS LIS Space Time Domain search result on 25 March 2023. The number of flashes in the area of interest (red box) is 33. Total number of flashes in the image is 117. Source: https://lightning.nsstc.nasa.gov/.

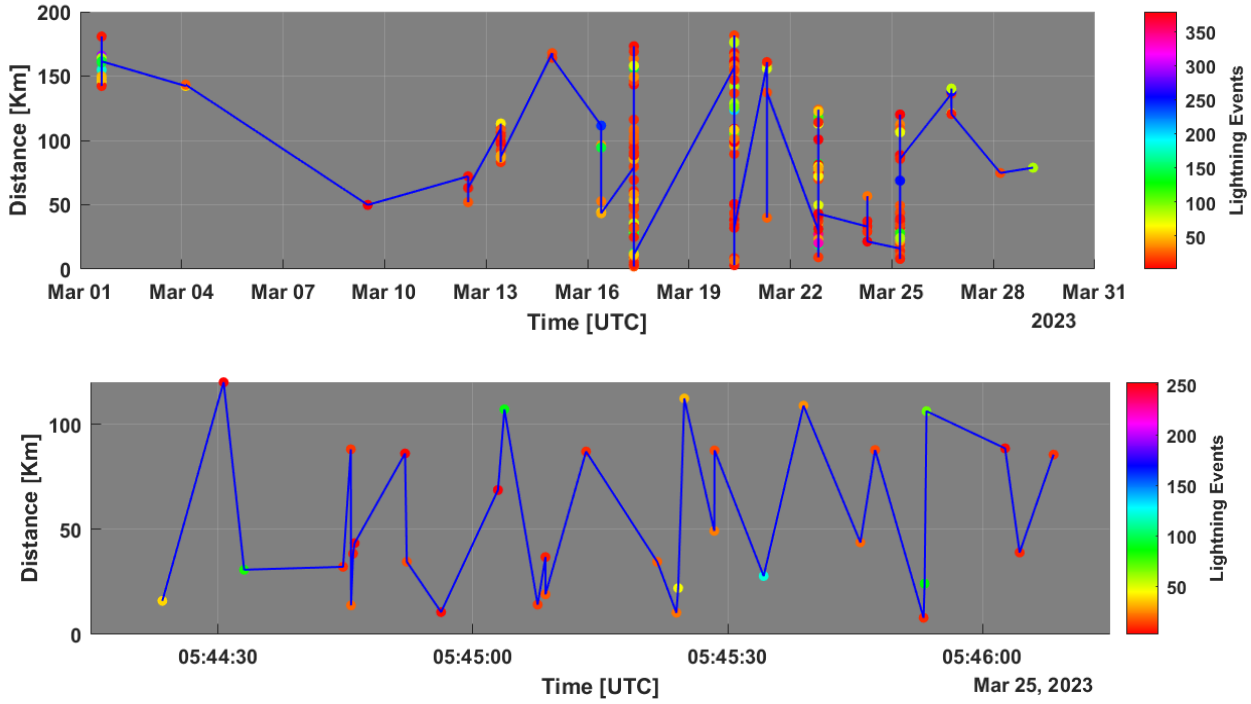

Figure 2. Time variation of lightning distance distribution per flash detection interval (colored dot shows the lightning event detected by the sensor on the observation of time inside the red rectangle of Figure-3). (Top) Lightning events detected on March 2023. (Bottom) Lightning events detected on March 25, 2023.

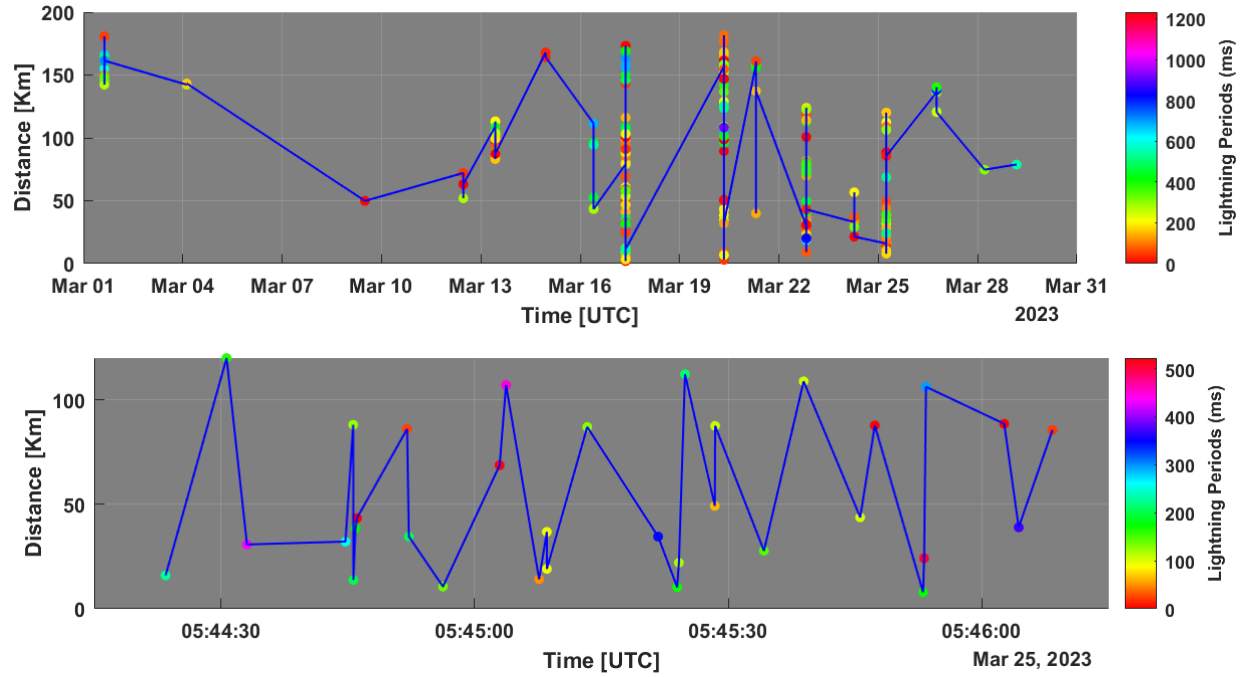

Figure 3. Time variation of lightning distance distribution per flash detection interval (colored dot shows the lightning period detected by the sensor on the observation of time inside the red rectangle of Figure 3). (Top) Lightning period detected in March 2023. (Bottom) Lightning period detected on March 25, 2023.

3. Observations

3.1. Infrasound from lightning

An infrasound wave detector system design that is low in cost, has minimal power consumption and is easy to carry was used for this study. The design and operating location of this system is provided in Figures 4 and 5. The detector system consists of a single board computer, infrasound sensor, Global Positioning System (GPS) and a display (Figure 4, left). A single board computer functions as the heart of controlling the performance of all systems. All components are joined in one network that is connected in the same Internet Protocol (IP) address configuration and synchronized by GPS. All components require relatively low electrical power. The system is operated in the city of Bandung, West Java (red triangle in Figure 5).

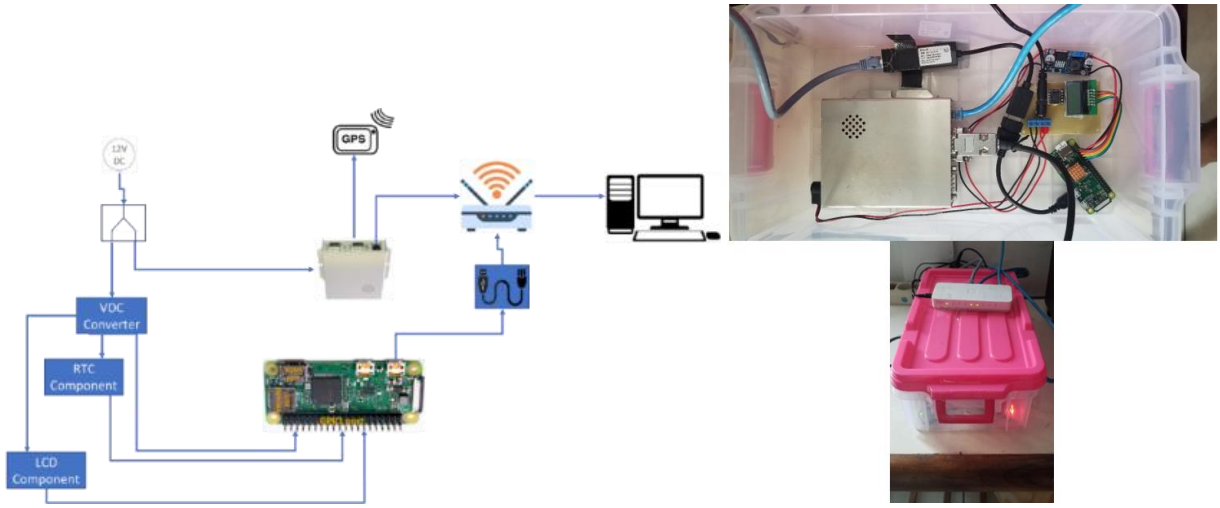

Figure 4. The system used during the observation of infrasound waves. Block diagram of the system (left). The image of the system used in the observation (right).

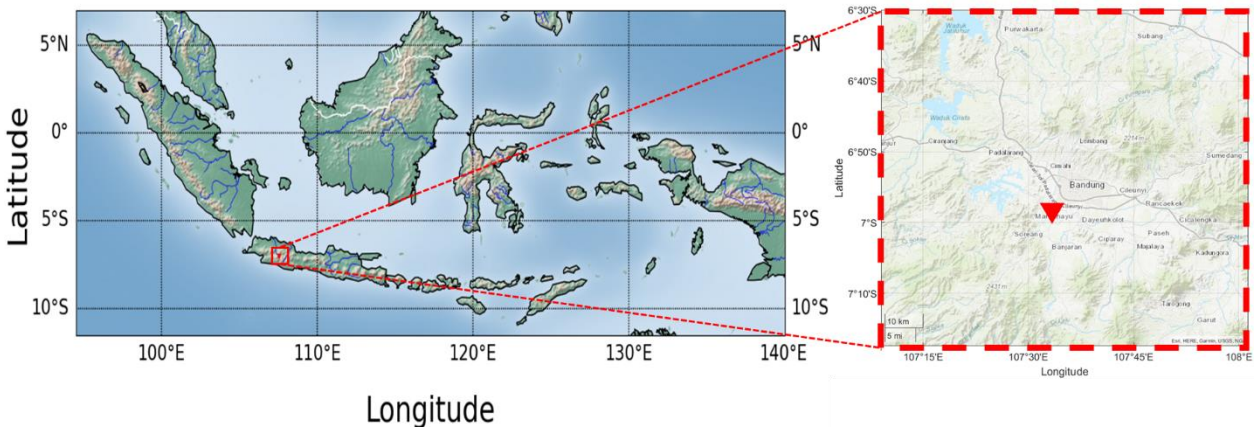

Figure 5. Map of the Indonesia archipelago. Red square shows the scope area of the observation site (left). The location of the observation site marked as red triangle inside the red dash square after zoom out (right).

On March 25, 2023, a severe thunderstorm passed directly through the West Java province of Indonesia, as shown in Figure 1. The periods before and after the target event were taken to explain the detection of lightning activity using an infrasound detector system. We recorded infrasound observation data for the period of the 10th of March to 31 March 2023. Figure 6 depicts the pattern of the observed infrasound signals during the period. The intensity of the amplitude of the signals observed during the day has accumulated, according to the results of infrasound observation in March 2023. For example, data on March 13th, 22nd and 25th of 2023 demonstrated that the observed wave strength density occurred between 10 and 04 Coordinate Universal Time (UTC). The recorded wave amplitude intensity was rarely witnessed the other day, and the thunderstorm did not occur at this time, as measured by the weather station (Figure 7, upper panel).

The infrasound signal is analyzed by a 1-D discrete Fourier transform (DFT). Each signal is slid iteratively based on the analysis window *g(n)* length $\boldsymbol{M}$. For each iteration, the next signal skips the previous signal by a window interval R, equivalent to $\boldsymbol{L = M - R}$ overlapping samples between adjacent segments. The spectrum of each windowed segment is added to a complex value matrix containing the magnitude and phase for each time point and frequency. So, the spectrum has $k = \left\lfloor \frac{N_x - L}{M - L} \right\rfloor$ columns, where N_x is the length of the signal $x(n)$ and the symbol $\lfloor \ \rfloor$ describes the floor function. The number of matrix rows equals N_{DFT}, with the number of DFT points for centered and two-sided transformations and an odd number close to $N_{DFT}/2$ for one-sided real-valued signal transformations. The *m-th* column of the spectrum matrix is $X(f) = [X_1(f)\ X_2(f)\ X_3(f) \cdots\ X_k(f)]$ which contains the DFT of *mR* time-centered windowed data: $X_m(f) = \sum_{n=-\infty}^{\infty} x(n)G(n - mR)e^{-j2\pi fn}$.

In order to confirm as well as to identify thunderstorm events, a spectral analysis of the time series data for infrasound wave observations was carried out. The results of the spectral profile of infrasound wave observation data in March 2023 is shown in Figure 8. The profile is displayed per day for every two minutes of the spectrum with 75% data overlap, window hamming and 1,024 spectral data (blue). The spectrum of each windowed segment is added to a complex value matrix containing the magnitude and phase for each time point and frequency. The red, green and yellow lines represent the values of the 90th, 50th and 10th percentile, respectively. These three percentile values are used to see the noise level of the infrasound signal. The first profile is the spectrogram contour for 24 hours on 25 March 2023 (Figure 9, bottom left). Meanwhile, the spectral profile accompanied by the three percentile level values, is shown in Figure 9 on the right panel. It can be seen that all of the recorded infrasound wave spectra show spectral similarities at frequencies around 10–12 Hz. It is suspected that this spectral range originates from the background noise around the observation station (e.q., wind speed). Besides that, the spectral source might be generated from wind speed noise around the observation area. On the other hand, from the spectral results of infrasound waves in March 2023, several spectral anomalies appeared in the two to three Hz frequency range. Specifically for the spectral profile on March 25th, 22nd and 13th of 2023, high lightning activity was detected by the ISS LIS. The three spectrum profiles on these three dates show the similarity of spectrum anomalies in the two to three Hz frequency range at the 90th, 50th and 10th percentile levels.

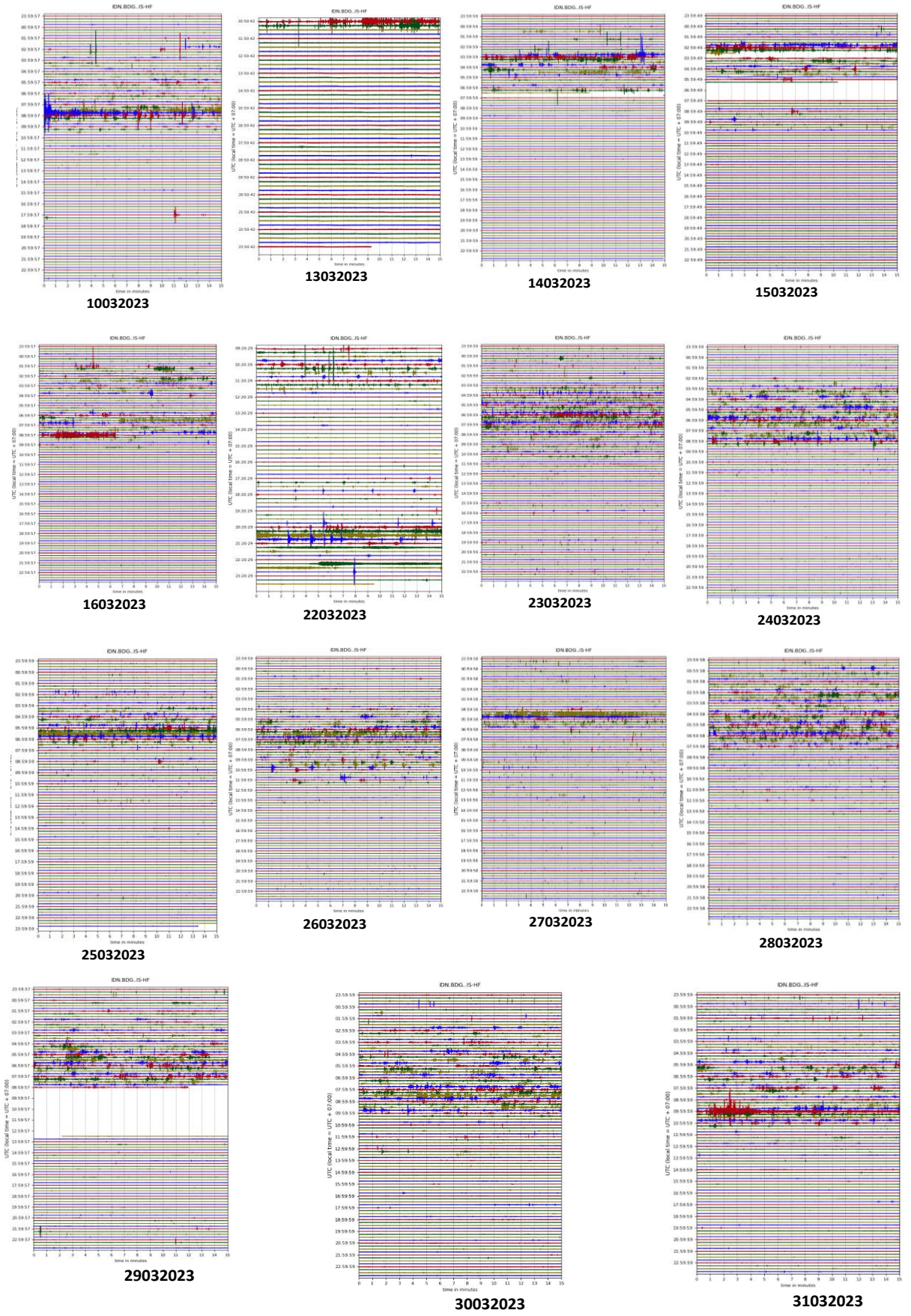

Figure 6. Infrasound waveform plot—day plot from the 10th–31st of March 2023.

It can be seen from the spectral contour of the infrasound signal that the spectral density is in the time range 04–07 UTC with the dominant frequency range up to 10 Hz. The unique thing is seen in the spectral profile with the percentile level: The spectral sensitivity at a frequency value of 10 Hz looks constant not only on March 15, 2023, but there is also an increase in the spectra at frequencies around 0.8–4 Hz, and this is thought to be the frequency spectra of thunderstorms. These results corroborate previous reports on the frequency range of infrasound signals associated with thunderstorm events [50–53].

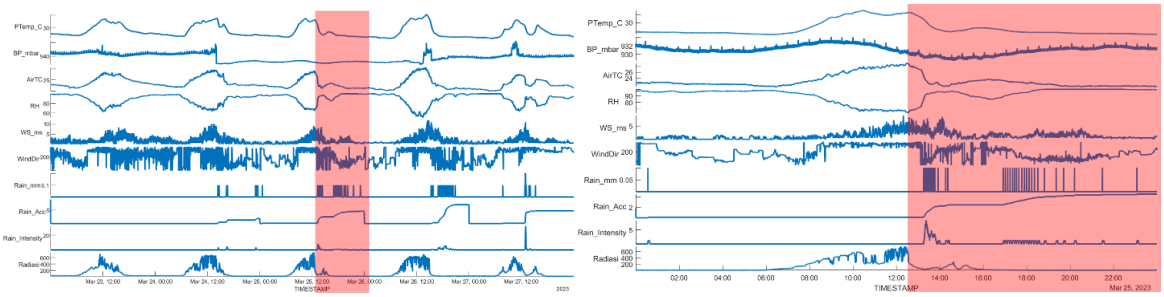

Figure 7. Meteorological state at the ground level from the AWS. Ten parameters of surface condition recorded by AWS.

The infrasound signal is also analyzed by spectral and percentile statistics for every one hour of observation. The results of this calculation can be seen in Figure 10. The spectral profile is calculated using the same formulation as the calculation of the one-day data spectra (Figure 6). The spectral anomaly occurs at a frequency of one to four Hz starting at 12 Local Time (LT), and this is in sync with the results of the lightning detection by the ISS LIS in Figure 1.

The thunderstorm on March 25, 2023 was detected by infrared detectors. Figure 11 depicts the profile of infrasound wave observation data collected while a thunderstorm passes over the infrasound station area. It is clear that a signal that is substantially stronger than the background levels peaks during the time when the thunderstorm appears and is accompanied by a considerable anomalous change in the output of the infrared wave at its low frequency level (Figure 11, upper left panel).

While rain has been confirmed with rainfall intensity, time tracking checks of wind speed and direction and measured radiation levels, it suggests that increased infrasound levels correlate with the mechanism of thunderstorm formation (Figure 7) accompanied by a strong surge of electrostatic energy [12,26–29]. This is also consistent with the fact that the sensor detected multiple pulse spikes during the time of the thunderstorm occurrence (Figure 11, right).

On the other hand, there is some convincing concrete evidence that thunderstorms are an active source of infrasound waves covering a wide altitude range from the troposphere to the thermosphere [54–56]. Data indicates electrostatic excitation of 0.1–4 Hz infrasound waves from thunderclouds and recently discovered high-frequency infrasound emission, which correlates with lightning-induced transient light events in the mesosphere [51–53].

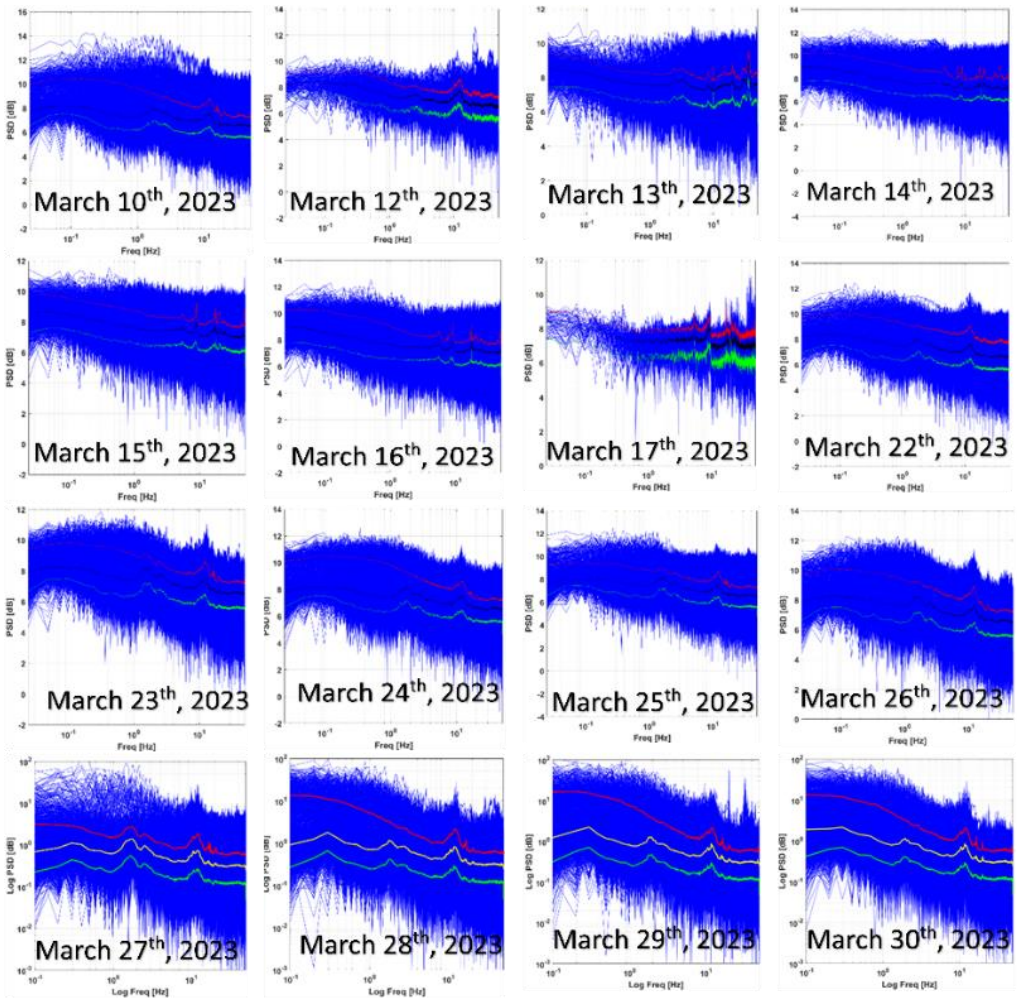

Figure 8. Infrasound wave spectrum profile in March 2023. The profile is displayed per day for every two minutes of the spectrum (blue). The red, green and yellow lines represent the values of the 90th, 50th and 10th percentile, respectively.

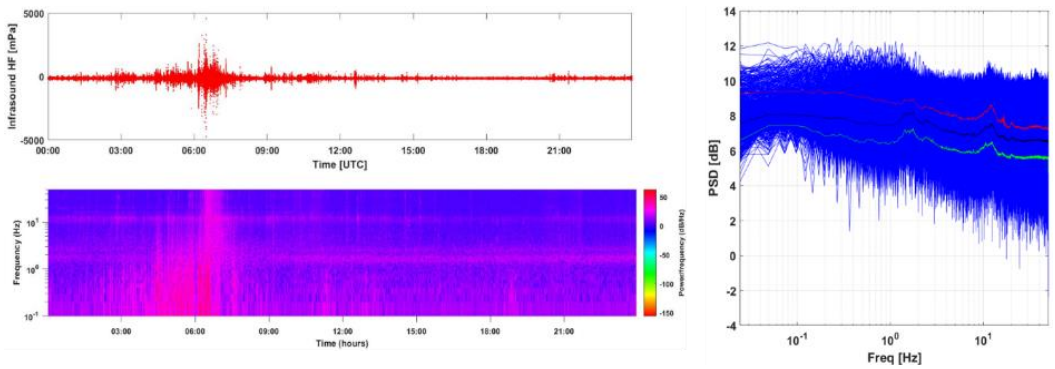

Figure 9. Infrasound spectra during the thunderstorm on March 25, 2023. Time series of infrasound signals on March 25, 2023 (top left panel). Infrasound signal spectrogram contours recorded on March 25, 2023 (bottom left panel). While the spectral profile is accompanied by the values of each 90% (red line), 50% (blue line) and 10% (yellow line) percentile of the spectral data (right panel).

In Bandung, the signal from the storm was successfully observed at the Bandung infrasound station on March 25, 2023 during observations in March 2023. Data analysis has identified the characteristics of infrasound fluctuations from thunderstorms (Figure 12, bottom panel). The signal wave structure of this profile can be illustrated by a sketched curve of a one-dimensional pressure perturbation model (Figure 12, top left). The N-shaped model of acoustic pressure pulses several meters from the channel associates the expansion of the air heated by the lightning discharge with its shock wave. The main point is the appearance of a rarefaction low pressure zone within the charged layer.

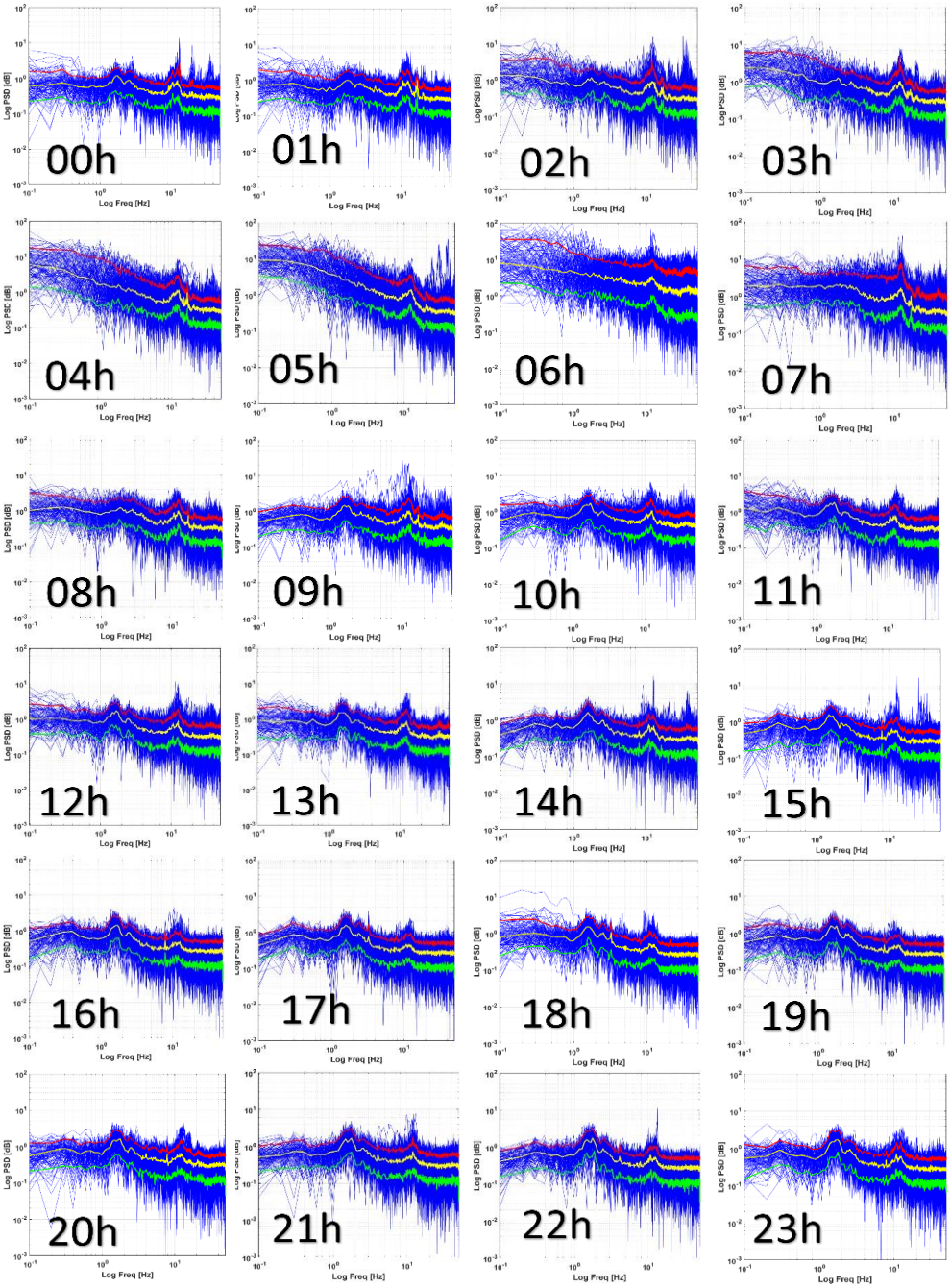

Figure 10. Spectral profile of infrasound waves for 24 hours of observation on March 25, 2023. The red, yellow and green lines indicate the 90%, 50% and 10% percentile values of a group of data. The blue plot explains the spectral infrasound data calculated every two minutes.

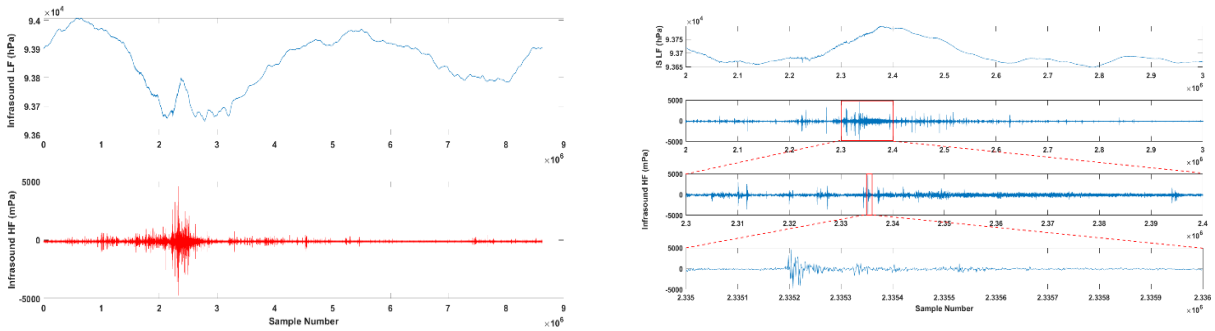

Figure 11. The measured sound pressure versus time in minutes relative to the thunderstorm (March 25, 2023) across the infrasound station.

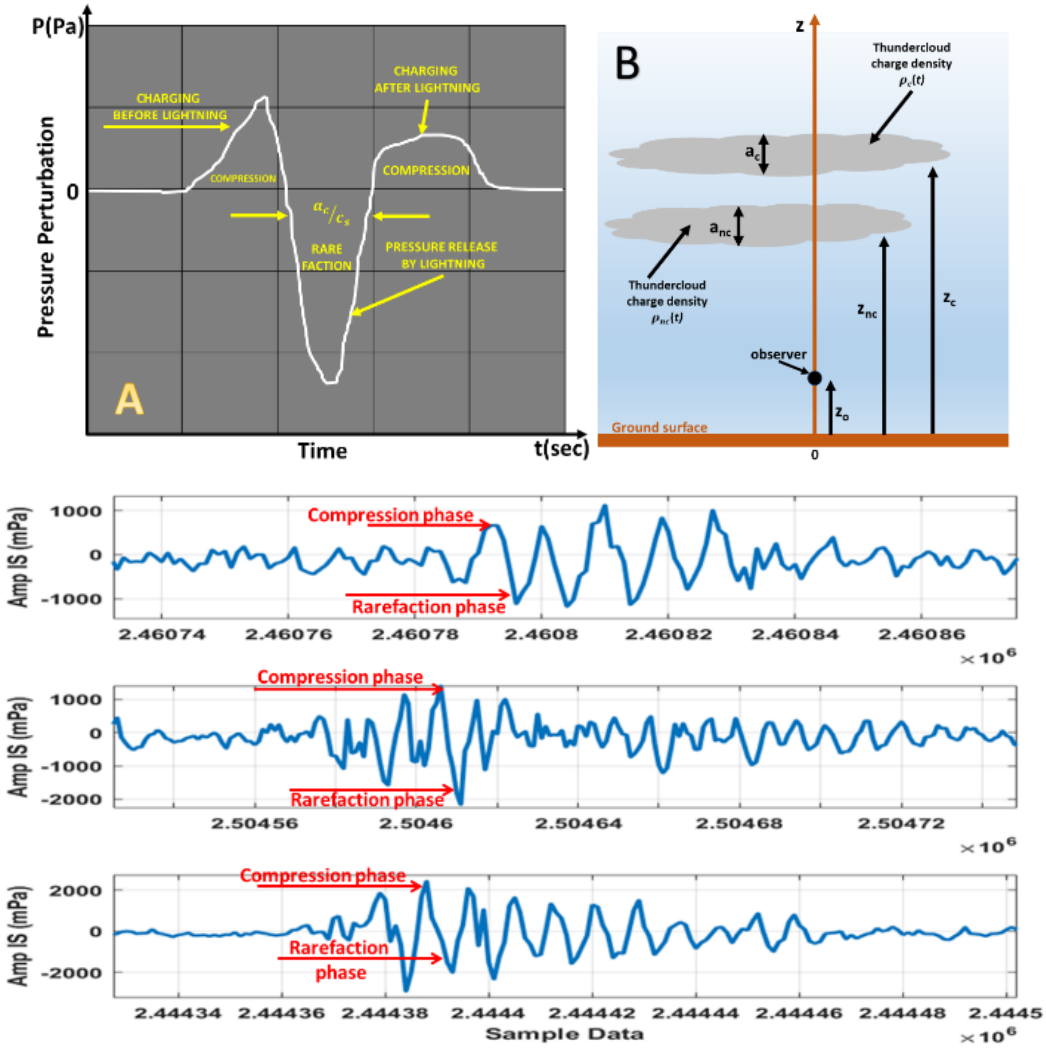

Figure 12. Sketched model of pressure perturbation of thunderstorm and interpretation of infrasound signal from thunderstorm. Infrasound waves from thunderstorm (March 25, 2023) with the structure of phase and the sequence rarefaction phase. Curve sketched of 1–D thundercloud model (A). Representation of multiple thundercloud model (B). Interpretation of infrasound signal from thunderstorm detected by infrasound station in Bandung on March 25, 2023 (bottom panel).

Infrasound signal as shown in Figure 12 (bottom panel) was a pulse with a multiple repeating structure with a clear negative pressure rarefaction phase. Thunderclouds in this case can be represented as multiple charged layers located near the level heights of z_c and z_{nc}, as shown in Figure 12 (top right panel), where z_c and z_{nc} are the heights of the thundercloud charged layers ρ_c and ρ_{nc}; a_c and a_{nc} are the thickness of the thundercloud charged layer; the interval duration of the rarefaction phase is determined by $\Delta t_c = {}^{a_c}/_{c_s}$ and $\Delta t_{nc} = {}^{a_{nc}}/_{c_s}$ which is the formation period of infrasound pulses in the charged layer a_c and a_{nc} respectively. In this case, c_s is the sound speed of the source. In our case, based on three samples of infrasound signals recorded at infrasound station from the thunderstorm event in Bandung, West Java on March 25, 2023 (Figure 12, bottom panel), it is possible to estimate the thickness of a thundercloud charged layer by the relation $a_{nc} = \Delta t_{nc} c_s$, where n is the integer number of infrasound pulses. Thus, the charged layer of a thundercloud accompanied by an electric field from the charged layer that generates infrasound waves can be estimated for its characteristic value based on the estimated characteristics of the infrasound signal.

3.2. Precipitation by weather radar

The weather radar named SANTANU was used in order to complement our data analysis. SANTANU is a monitoring system for local scale rain monitoring as an alternative technology to fill in areas that are not monitored by existing weather radar. SANTANU is an x band rain scanner based on marine radar development. This radar has a wide vertical beam that could scan a very large volume of precipitation. The name Santatnu was chosen from a puppet character in the Mahabarata story. A clutter map was applied to extract the ground clutter in order to achieve the precipitation data [57]. Spatial and temporal resolution are 240 × 240 meters in every two minutes. High temporal resolution can be utilized to analyze the precipitation movement, and also the rate of growth/decay area of precipitation [57]. The observation area was focused in the Bandung Basin in West Java, Indonesia. Radar data used in this work has been uploaded in the repository of National Research and Innovation Agency of Indonesia (BRIN), https://data.brin.go.id/dataset.xhtml?persistentId=hdl:20.500.12690/RIN/FB934H.

The results of the SANTANU radar observations, especially when a thunderstorm occurs, can be seen in Figure 13 where the reflectivity radar contours are in dBz. Radar reflectivity data was analyzed for a storm of interest on March 25, 2023. SANTANU was detecting precipitation from 12.00 LT until 14:40 LT (Figure 13). Various precipitation objects were observed during those periods. Heavy rainfall occurred in the middle of the Bandung area from 13.10 until 14.40 LT. Twenty minutes later, heavy precipitation was also observed in almost every coverage area of the SANTANU. Precipitation clouds started to grow east of SANTANU until they filled the SANTANU observation area and the infrasound station. A severe thunderstorm began to pass over the infrasound station area at 13:22 LT to 13:30 LT. Ten minutes later, the cloud of precipitation gradually dissipated. During approximately eight minutes of intense thunderstorms above the infrasound station area, the sensors managed to detect infrasound waves generated from thunderstorms (Figure 13).

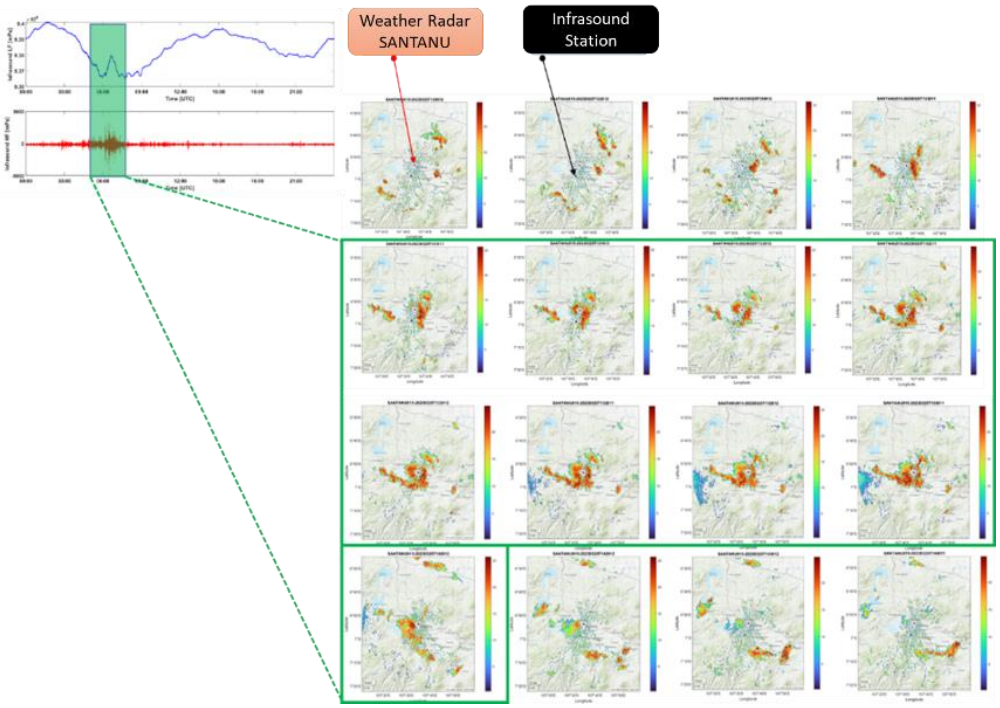

Figure 13. Radar reflectivity (right panel) corresponds to the infrasound signal due to thunderstorm (left panel). Radar reflectivity in unit of dBZ from weather station near the AWS system at 12 to 15 LT on March 25, 2023.

3.3. Meteorological conditionos at the ground

The atmospheric condition at ground level was observed by the automatic weather station (AWS) located at Bandung, West Java Indonesia. The AWS provides five minutes of recorded of wind speed and direction, rainfall, temperature, humidity and atmospheric pressure. The rainfall data is first quality-controlled and then processed to identify thunderstorm events. Data for our analysis is stored in a BRIN repository, https://data.brin.go.id/dataset.xhtml?persistentId=hdl:20.500.12690/RIN/4EMZYB.

The AWS station at Bandung was used to characterize the atmospheric condition at the ground level before and after the occurrence of the thunderstorm. The station recorded ten atmospheric conditions at the ground level before and after the thunderstorm passing through and above the station, provided in Figure 6 with the red rectangle showing the thunderstorm event (March 25, 2023). It can be seen in the bottom-right image that during a thunderstorm, the rain intensity gradually increases, followed by strong winds blowing south from the observation and humidity levels increasing. The AWS observation results were clarified by weather radar observations installed adjacent to the AWS station. Meanwhile, the radiation level dropped to around 400 levels, and the level of atmospheric pressure conditions on the surface was still at a level of around 930 milibar (mbar) after the drop fell around 10 mbar the day before the thunderstorm passed. Just before the thunderstorm formed, the atmospheric pressure decreased by two mbar, followed by a decrease in the level of detectable radiation.

The quality control and storm recognition are carried as follows: (1) The temporal continuity and extreme value of the five-minute interval rainfall series are examined. Records with five-minute

rainfall exceeding 40 mm are regarded as false values and eliminated. Only rainfall series with no missing or false values are used in the following storm identification. (2) When the five-minute cumulated rainfall of a particular AWS is greater than 0.1 mm and the subsequent one-hour rainfall exceeds five mm, this moment is defined as the beginning time of a storm event on this AWS. A storm event is considered to end when the subsequent one-hour accumulated rainfall is less than five mm. (3) After the storm events are identified, they are classified into different grades according to their rainfall intensity. In this study, different statistic characteristics are found when the mean rainfall rate during the storm is considered. Therefore, storm events are graded in two different ways: Mean rainfall rate (0–50, and ≥50 mm h−1) and rainfall intensity (0–2, 2–4, and ≥4). This provides us with a better understanding of the relationship between rainfall and lightning in storm events with different intensity.

4. Discussions

It is known that during a thunderstorm, the generation of low-frequency sound waves causes disturbances in the surrounding atmosphere. Infrasound waves produced by thunderstorms propagate along the atmosphere and can be observed several minutes later by sensors. The disturbance caused by thunderstorms of acoustic origin are N-shaped, with an initial overpressure half cycle with a relatively fast rise time and slower pressure decay followed by a smoothing half cycle [58]. The infrasound part of thunder can be attributed to the transformation of the electrostatic field of a thundercloud into sound. For instance, in the former case, the expansion of air heated by a lightning discharge with a shock wave transformed into an acoustic N-shaped pressure pulse at a distance of several meters from the channel [59,60].

Infrasonic events are identified as being generated by inversion-driven thunderstorms, which take on the spatial characteristics of the infrasound source. With the results of this study, we clearly demonstrate that infrasound from lightning can be measured and identified clearly. Lightning detection using infrasound measurements is mainly limited to sources located within 110 km of the station, even if infrasound from lightning located outside this distance can sometimes be detected in conditions of low background noise. Correlation with individual lightning discharges is possible at ranges shorter than 110 km and depends on the relative location of lightning within the storm (Figures 2 and 3).

The question of the mechanism of infrasound generation from lightning still needs to be addressed. Dessler's theory requires that the infrasound emission pattern from lightning is strongly oriented in the vertical direction and that its amplitude is proportional to the charge neutralized by the discharge. Wave propagation should then be restricted to planes close to the emission pattern. Infrasound detection of lightning beyond a few tens of kilometers from a thundercloud does not support this theory. Infrasound from lightning is more likely the infrasound counterpart of the acoustic emission of thunder. However, Dessler's theory can be involved in some cases and explain some of the infrasound signals correlated with lightning discharges near stations (e.g., Figure 12).

Surface meteorological observations provide a real picture of the impact of thunderstorms on the atmosphere at the surface. The significant change that was affected was the intensity of solar radiation, which fell by almost 80%.

5. Conclusions

This work presented infrasonic measurements during a lightning-producing thunderstorm in Bandung in March 2023. Lightning was investigated using ground-based weather radar, weather stations and infrasonic sensors, as well as satellite-based ISS LIS measurements. It was most likely that short duration infrasonic pulses were detected when the storm was within 100 km. During a thunderstorm, the noise level increased so that most of the infrasound from lightning was generated by the same mechanisms as audible thunder. The infrasonic spectrum of a single lightning strike is relatively flat, but includes several peaks around the one to four Hz frequency range. A simple pattern of pressure perturbation of thunderstorms can be used for the study of infrasonic pressure from thunderstorms where the main characteristics of this type of infrasonic are given, including its infrasonic spectrum and the law of amplitude change. The lightning discharge mechanism is a real natural event to evaluate and test models of changes in infrasonic atmospheric pressure around the station. Measurements of the intensity and frequency of lightning events, related to lightning timing and source distance, were provided by the ISS LIS, which is equipped with estimates of precipitation levels based on weather radar reflectivity and the projected effects of thunderstorms measured by weather stations on the surface. Regarding infrasonic from lightning, the activity of flashes is more than 2,000 activities detected in the image area and 258 flashes of activity detected in the area of interests during one month of observation in March 2023. When a thunderstorm passed over the infrasound observation site, the LIS sensor on the ISS satellite simultaneously detected some lightning activity in the infrasound wave observation area. The number of flashes in the area of interest was 33, and the total number of flashes in the image was 117. While the period of detected lightning events was 252 milliseconds for the longest period with the average value of the detected lightning pulse period being around 182.54 milliseconds, during a thunderstorm, fundamental frequencies up to four Hz were observed. The observed spectral peak appeared at 12 LT relative to the thunderstorm, which was confirmed by all three weather radar observations, weather stations and ISS LIS. Finally, the combination of the infrasonic with weather radar, weather station and ISS LIS provided insights about infrasonic and its relationship to thunderstorm events accompanied by lightning.

Use of AI tools declaration

The authors declare they have not used Artificial Intelligence (AI) tools in the creation of this article.

Acknowledgments

The authors would like to thank the Laboratory member of Kochi University of Technology (KUT), Japan, who originally set up the infrasonic sensor. This work was supported by a research grant of the National Research and Innovation Agency (BRIN). The research grants are provided by the Research Organization of Aeronautics and Space as well as the Research Organization of Disaster and Maritim—BRIN.

Conflict of interest

All authors declare no conflicts of interest regarding this study.

References

1. Lyons JJ, Haney MM, Fee D, et al. (2019) Infrasound from giant bubbles during explosive submarine eruptions. *Nat Geosci* 12: 952– 958. https://doi.org/10.1038/s41561-019-0461-0
2. Johnson JB, Ripepe M (2011) Volcano infrasound: A review. *J Volcanol Geotherm Res* 206: 61–69. https://doi.org/10.1016/j.jvolgeores.2011.06.006
3. Fee D, Matoza RS (2013) An overview of volcano infrasound: From hawaiian to plinian, local to global. *J Volcanol Geotherm Res* 249: 123–139. https://doi.org/10.1016/j.jvolgeores.2012.09.002
4. Matoza RS, Hedlin MAH, Garces MA (2007) An infrasound array study of Mount St. Helens. *J Volcanol Geotherm Res* 160: 249–262. https://doi.org/10.1016/j.jvolgeores.2006.10.006
5. Matoza RS, Fee D, Garcés MA, et al. (2009) Infrasonic jet noise from volcanic eruptions. *Geophys Res Lett* 36: L08303. https://doi.org/10.1029/2008GL036486
6. Cook RK (1971) Infrasound Radiated During the Montana Earthquake of 1959 August 18. *Geophys J R Astron Soc* 26: 191–198. https://doi.org/10.1111/j.1365-246X.1971.tb03393.x
7. Mutschlecner JP, Whitaker RW (2005) Infrasound from earthquakes. *J Geophys Res* 110: D01108. https://doi.org/10.1029/2004JD005067
8. Arrowsmith SJ, Whitaker R, Taylor SR, et al. (2008) Regional monitoring of infrasound events using multiple arrays: Application to Utah and Washington State. *Geophys J Int* 175: 291–300. https://doi.org/10.1111/j.1365-246X.2008.03912.x
9. Johnson JB, Mikesell TD, Anderson JF, et al. (2020) Mapping the sources of proximal earthquake infrasound. *Geophys Res Lett* 47. https://doi.org/10.1029/2020GL091421
10. Arrowsmith SJ, Burlacu R, Pankow K, et al. (2012) A seismoacoustic study of the 2011 January 3 Circleville earthquake: Seismoacoustic study: Circleville earthquake. *Geophys J Int* 189: 1148–1158. https://doi.org/10.1111/j.1365-246X.2012.05420.x
11. Le Pichon A, Herry P, Mialle P, et al. (2005) Infrasound associated with 2004–2005 large Sumatra earthquakes and tsunami. *Geophys Res Lett* 32: L19802. https://doi.org/10.1029/2005GL023893
12. Lin TL, Langston CA (2007) Infrasound from thunder: A natural seismic source. *Geophys Res Lett* 34: L14304. https://doi.org/10.1029/2007GL030404
13. Chimonas G (1977) A possible source mechanism for mountain-associated infrasound. *J Atmos Sci* 34: 806–811. https://doi.org/10.1175/1520-0469(1977)034%3C0806:APSMFM%3E2.0.CO;2
14. Hupe P (2018) Global infrasound observations and their relation to atmospheric tides and mountain waves. Ph.D. thesis, Ludwig-Maximilians-Universität München, Germany. Available from: https://edoc.ub.uni-muenchen.de/23790/
15. Le Pichon A, Ceranna L, Pilger C, et al. (2013) The 2013 Russian fireball large ever detected by CTBTO infrasound sensors. *Geophys Res Lett* 40: 3732–3737. https://doi.org/10.1002/grl.50619
16. Landes M, Ceranna L, Le Pichon A, et al. (2012) Localization of microbarom sources using the IMS infrasound network. *J Geophys Res* 117: D06102. https://doi.org/10.1029/2011JD016684
17. Arrowsmith SJ, Hedlin, MAH, Stump B, et al. (2008) Infrasonic Signals from Large Mining Explosions. *Bull Seismol Soc Amer* 98. https://doi.org/10.1785/0120060241

18. Bowman DC, Krishnamoorthy S (2021) Infrasound from a buried chemical explosion recorded on a balloon in the lower stratosphere. *Geophys Res Lett* 48: e2021GL094861. https://doi.org/10.1029/2021GL094861
19. Il-Young Che, Park J, Kim I, et al. (2014) Infrasound signals from the underground nuclear explosions of North Korea. *Geophys J Int* 198: 495–503. https://doi.org/10.1093/gji/ggu150
20. Applbaum, D, Averbuch G, Price C, et al. (2019) Infrasound observations of sprites associated with winter thunderstorms in the eastern mediterranean. *Atmos Res* 235: 104770. https://doi.org/10.1016/j.atmosres.2019.104770
21. Campus P, Christie DR (2010) Worldwide Observations of Infrasonic Waves, In: Le Pichon A, Blanc E, Hauchercorne A. (eds), *Infrasound Monitoring for Atmospheric studies*, Springer Netherlands, 185–234. https://doi.org/10.1007/978-1-4020-9508-5_6
22. Christie DR, Campus P (2010) The IMS Infrasound Network: Design and Establishment of Infrasound Stations, In: Le Pichon A, Blanc E, Hauchercorne A, (eds), *Infrasound Monitoring for Atmospheric studies*, Springer Netherlands. 29–75. https://doi.org/10.1007/978-1-4020-9508-5_2
23. Batubara M, Yamamoto MY (2020) Infrasound Observations of Atmospheric Disturbances Due to a Sequence of Explosive Eruptions at Mt. Shinmoedake in Japan on March 2018. *Remote Sens* 12: 728. https://doi.org/10.3390/rs12040728
24. Houghton HG (1951) On the Physics of Clouds and Precipitation. In: Malone TF, (eds), *Compendium of Meteorology.* American Meteorological Society, Boston, MA. https://doi.org/10.1007/978-1-940033-70-9_14
25. Gaskell W (1981) A laboratory study of the inductive theory of thunderstorm electrification. *Quart J Roy Meteor Soc* 107: 955–966. https://doi.org/10.1002/qj.49710745413
26. Gilmore MS, Straka JM, Rasmussen EN (2004) Precipitation and evolution sensitivity in simulated deep convective storms: Comparisons between liquid-only and simple ice and liquid phase microphysics. *Mon Weather Rev* 132: 1897–1916. https://doi.org/10.1175/1520-0493(2004)132<1897:PAESIS>2.0.CO;2
27. Jayaratne ER, Saunders CPR (1985) Thunderstorm electrification: The effect of cloud droplets. *J Geophys Res* 90: 13063–13066. https://doi.org/10.1029/JD090iD07p13063
28. Lang TJ, Jay Miller L, Weisman M, et al. (2004) The Severe Thunderstorm Electrification and Precipitation Study. *Bull Amer Meteor Soc* 85: 1107–1126. https://doi.org/10.1175/BAMS-85-8-1107
29. Pereyra RG, Avila EE, Castellano NE, et al. (2000) A laboratory study of graupel charging. *J Geophys Res* 105: 20803–20812. https://doi.org/10.1029/2000JD900244
30. Qie X, Yuan S, Chen Z, et al. (2021) Understanding the dynamical-microphysical-electrical processes associated with severe thunderstorms over the Beijing metropolitan region. *Sci China Earth Sci* 64: 10–26. https://doi.org/10.1007/s11430-020-9656-8
31. Reynolds SE, Brook M, Gourley MF (1957) Thunderstorm charge separation. *J Atmos Sci* 14: 426–436. https://doi.org/10.1175/1520-0469(1957)014<0426:TCS>2.0.CO;2
32. Saunders CPR (1993) A review of thunderstorm electrification processes. *J Appl Meteor Climatol* 32: 642–655. https://doi.org/10.1175/1520-0450(1993)032<0642:AROTEP>2.0.CO;2
33. Takahashi T (1978) Riming electrification as a charge generation mechanism in thunderstorms. *J Atmos Sci* 35: 1536–1548. https://doi.org/10.1175/1520-0469(1978)035<1536:REAACG>2.0.CO;2

34. Wang X, Liao R, Li J, et al. (2020) Thunderstorm identification algorithm research based on simulated airborne weather radar reflectivity data. *J Wireless Com Network* 37. https://doi.org/10.1186/s13638-020-1651-6
35. Petersen WA, Rutledge SA (1998) On the relationship between cloud-to-ground lightning and convective rainfall. *J Geophys Res* 103: 14025–14040. https://doi.org/10.1029/97JD02064
36. Price C, Federmesser B (2006) Lightning-rainfall relationships in Mediterranean winter thunderstorms. *Geophys Res Lett* 33: L07813. https://doi.org/10.1029/2005GL024794
37. Blakeslee R, Koshak W (2016) LIS on ISS: Expanded Global Coverage and Enhanced Applications. *Earth Obs* 28: 4–14.
38. Blakeslee RJ, Lang TJ, Koshak WJ, et al. (2020) Three Years of the Lightning Imaging Sensor Onboard the International Space Station: Expanded Global Coverage and Enhanced Applications. *J Geophys Res Atmos* 125: e2020JD032918. https://doi.org/10.1029/2020JD032918
39. Baldini L, Roberto N, Montopoli M, et al. (2018) Ground-Based Weather Radar to Investigate Thunderstorms. In: Andronache C, (eds), *Remote Sensing of Clouds and Precipitation*. Springer Remote Sensing/Photogrammetry. Springer, Cham. https://doi.org/10.1007/978-3-319-72583-3_4
40. Hwang SH, Kim KB, Han D (2020) Comparison of methods to estimate areal means of short duration rainfalls in small catchments, using rain gauge and radar data. *J Hydrol* 588: 125084. https://doi.org/10.1016/j.jhydrol.2020.125084
41. Prajapati R, Silwal P, Duwal S, et al. (2022) Detectability of rainfall characteristics over a mountain river basin in the Himalayan region from 2000 to 2015 using ground-and satellite-based products. *Theor Appl Climatol* 147: 185–204. https://doi.org/10.1007/s00704-021-03820-9
42. Wu F, Cui X, Zhang DL, et al. (2017) The relationship of lightning activity and short-duration rainfall events during warm seasons over the Beijing metropolitan region. *Atmos Res* 195: 31–43. https://doi.org/10.1016/j.atmosres.2017.04.032
43. Williams E, Mkrtchyan H, Mailyan B, et al. (2022) Radar diagnosis of the thundercloud electron accelerator. *J Geophys Res Atmos* 127: e2021JD035957. https://doi.org/10.1029/2021JD035957
44. Uman MA (2001) *The lightning discharges*, Courier Corporation.
45. Rakov VA, Uman MA (2003) *Lightning, Physics and Effects*, Cambridge University Press, New York. 687. https://doi.org/10.1017/CBO9781107340886
46. Few AA, Teer TL (1974) The accuracy of acoustic reconstructions of lightning channels. *J Geophys Res* 79: 5007–5011. https://doi.org/10.1029/JC079i033p05007
47. MacGorman DR, Few AA, Teer TL (1981) Layered lightning activity. *J Geophys Res* 86: 9900–9910. https://doi.org/10.1029/JC086iC10p09900
48. Hagenguth JH (1951) The Lightning Discharge. In: Malone TF, Eds., *Compendium of Meteorology.* American Meteorological Society, Boston, MA. https://doi.org/10.1007/978-1-940033-70-9_11
49. Dessler AJ (1973) Infrasonic thunder. *J Geophys Res* 78: 1889–1896. https://doi.org/10.1029/JC078i012p01889
50. Pasko VP (2009) Mechanism of lightning associated infrasonic pulses from thunderclouds. *J Geophys Res* 114: D08205. https://doi.org/10.1029/2008JD011145
51. Liszka L (2004) On the possible infrasound generation by sprites. *J Low Freq Noise V A* 23: 85–93. https://doi.org/10.1260/0263092042869838

52. Farges T, Blanc E, le Pichon A, et al. (2005) Identification of infrasound produced by sprites during the Sprite2003 campaign. *Geophys Res Lett* 32: L01813. https://doi.org/10.1029/2004GL021212
53. Liszka L, Hobara Y (2006) Sprite-attributed infrasonic chirps—Their detection, occurrence and properties between 1994 and 2004. *J Atmos Solar-Terr Phys* 68: 1179–1188. https://doi.org/10.1016/j.jastp.2006.02.016
54. Blanc E (1985) Observations in the upper atmosphere of infrasonic waves from natural or artificial sources: A summary. *Ann Geophys* 3: 673–688.
55. Few AA (1995) *Acoustic radiations from lightning. Handbook of Atmospheric Electrodynamics*, CRC Press, Boca Raton, 1–31. https://doi.org/10.1201/9780203713297
56. Drob DP, Picone JM, Garces M (2003) Global morphology of infrasound propagation. *J Geophys Res* 108: 4680. https://doi.org/10.1029/2002JD003307
57. Nugroho GA, Sinatra T, Fathrio I (2018) Application of rain scanner SANTANU and transportable weather radar in analyze of Mesoscale Convective System (MCS) events over Bandung, West Java. *IOP Conf Ser Earth Environ Sci* 149: 012058. https://iopscience.iop.org/article/10.1088/1755-1315/149/1/012058
58. Zel'dovich YB, Raizer YP (2002) *Physics of shock waves and high-temperature hydrodynamic phenomena*, Academic Press, New York & London.
59. Few AA (1982) *Acoustic radiations from lightning. Handbook of Atmospherics*, CRC Press, Inc., Boca Raton, 257–289.
60. Few AA (1985) The production of lightning-associated infrason ic acoustic sources in thunderclouds. *J Geophys Res* 90: 6175–6180. https://doi.org/10.1029/JD090ID04P06175

AIMS Press